

Biocompatible technique for nanoscale magnetic field sensing with Nitrogen-Vacancy centers

E. Bernardi¹, E. Moreva¹, P. Traina¹, G. Petrini^{2,1}, S. Ditalia Tchernij², J. Forneris^{2,3}, Ž. Pastuović⁴, I. P. Degiovanni^{1,3}, P. Olivero^{2,3,1}, M. Genovese^{1,3}.

¹*Istituto Nazionale di Ricerca Metrologica, Strada delle cacce 91, Torino, Italy*

²*Physics Department and NIS Centre of Excellence - University of Torino, Torino, Italy*

³*Istituto Nazionale di Fisica Nucleare (INFN) Sez. Torino, Torino, Italy and*

⁴*Centre for Accelerator Science, Australian Nuclear Science and Technology Organisation, New Illawarra rd., Lucas Heights, NSW 2234, Australia*

We present an innovative experimental set-up that uses Nitrogen-Vacancy centres in diamonds to measure magnetic fields with the sensitivity of $\eta = 59.6 \pm 1.3 \text{ nT}/\sqrt{\text{Hz}}$ at demonstrated nanoscale. The presented method of magnetic sensing utilizing the ODMR technique for the optical detection of microwave-driven spin resonances induced in NV centres, which are highly concentrated to a nanoscaled volume probed by focused laser light, is characterized by the excellent magnetic sensitivity at such small scale and the full biocompatibility. As such, this method offers a whole range of research possibilities for biosciences. We also report how the magnetic sensitivity changes for different applied laser power and discuss the limits of the sensitivity sustainable with biosystem at such small volume scale.

PACS numbers: 42.50.-p; 71.55-i;

Magnetometry in biological systems is of the utmost importance for fundamental biological science and medicine. Mapping brain activity by recording magnetic fields produced by the electrical currents which are naturally occurring in the brain is of extreme interest^{1,2}, with direct applications in the timely detection and cure of psychic and neurodegenerative disorders^{3,5,6}. Measuring the magnetic fields produced by electrical currents in the heart is also of the utmost importance⁷, since this also could lead to a new generation of non-invasive diagnostic and therapeutic techniques⁸. Superconductive quantum interference device (SQUID) magnetometers are usually used for both these kinds of measurements. Nonetheless, the significant drawbacks of SQUID magnetometers are represented by the facts that they are unable to sense to single nerve impulses, and they are costly, bulky, and require cryogenic refrigeration^{9,10}.

Magnetometers based on Nitrogen-Vacancy(NV) centers in diamond represent a valid alternative to SQUID-based magnetometry. Firstly, diamond offers the substantial advantage of being fully biocompatible^{6,11-15}. On the other side, NV centers are characterized by a peculiar electronic level structure that allows the optical detection of their microwave-driven spin resonances with a technique referred as Optically Detected Magnetic Resonance(ODMR)¹⁶⁻¹⁹. The shift in the ODMR frequency is related to the projection of the local magnetic field along the NV center axis. If an ensemble of NV centers is used, it is possible to reconstruct the 3D structure of the field, taking advantage of the 4-different possible orientations of the NV axis within the surrounding crystal structure.²⁰.

NV magnetometry has already been exploited to detect the action potential in a macroscopic biological sample²¹. In this proof-of-principle experiment, Barry and coworkers achieved a magnetic field sensitivity of

$\eta = 15 \pm 1 \text{ pT}/\sqrt{\text{Hz}}$ with a sensing volume, i.e.the volume containing the ensemble of the excited centers, of $(13 \times 2000 \times 2000) \mu\text{m}^3$ and optical power of 2.75 - 4.5 W. To extend NV-based-biomagnetometry from macroscopic samples to small tissues up to single cells, a smaller sensing volume and a lower optical power should be used. The characteristic size of a cell is approximately $10 \mu\text{m}$, and the laser power used in confocal measurement on living cells reported in²² is in the range of few mW.

In this work, we present a NV-magnetometry protocol characterized by a sensing volume of $(0.01 \times 10 \times 10) \mu\text{m}^3$ and optical powers from 2.5 mW to 80 mW, values compatible, as we will discuss, with magnetometry at the cellular level.

I. EXPERIMENTAL SETUP

The application of a magnetic field removes the energy degeneracy between the $m_S = \pm 1$ spin states, and the frequency difference $\nu_+ - \nu_-$ between the two ODMR dips is proportional to the component B_{NV} of the field along the NV-axis:

$$\nu_+ - \nu_- = \frac{1}{h} 2g\mu_B B_{NV} \quad (1)$$

where g is the Landé factor and μ_B the Bohr magneton. A variation δB_{NV} in the applied magnetic field causes a shift $\delta\nu_+ = \frac{1}{h} g\mu_B \delta B_{NV}$ to the higher-frequency ODMR dip and a corresponding $\delta\nu_- = -\frac{1}{h} g\mu_B \delta B_{NV}$ shift for the lower-frequency one. Tracking the ODMR shift $\delta\nu_+$ allows the measurement of the variation of the applied field δB_{NV} .

The simplest way to track the ODMR shift is to collect the photoluminescence signal while scanning the microwave frequency. Adopting a frequency modulation

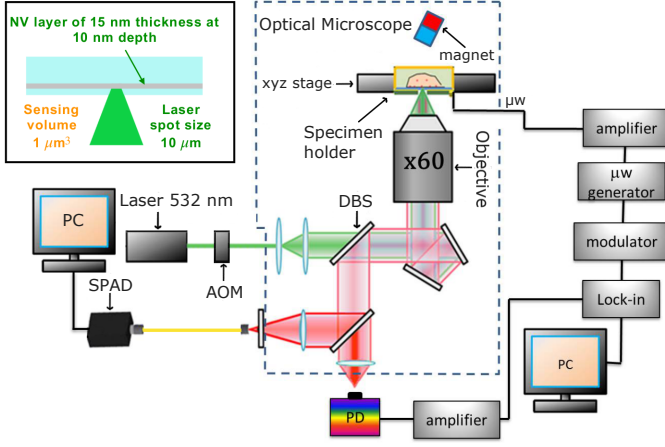


FIG. 1: Schematics of the experimental set-up. The optical excitation using a green laser, the microwave (μW) control and the lock-in detection are depicted. In the inset a drawing of the sample is shown.

of the microwaves can improve this method: the modulating signal is centered at the resonance dip and has an amplitude equal to the full-width half maximum of the resonance²³. The resulting modulated photoluminescence signal is read by a lock-in amplifier (LIA).

Figure 1 depicts the experimental set-up: the diamond sensor, laser excitation system, the microwave generation and LIA detection apparatus. The diamond sample was mounted on a microwave planar ring antenna, specifically designed for ODMR measurements in a 400 MHz frequencies range centered around the 2.87 GHz spin resonance²⁴.

The sensor consisted of a $3 \times 3 \times 0.3 \text{ mm}^3$ diamond substrate produced by Element Six by CVD deposition, having $< 1 \text{ ppm}$ and $< 0.05 \text{ ppm}$ concentrations of substitutional nitrogen and boron, respectively. The substrate incorporates a $\sim 10 \text{ nm}$ thick layer of NV centers at a concentration of $n_{\text{NV}} \sim 3 \cdot 10^{19} \text{ cm}^{-3}$, see inset of Fig. 1, that was produced by low-energy N ion irradiation followed by high temperature annealing.

The excitation light (80 mW optical power) at 532 nm was obtained by the second harmonic of a Nd:YAG laser with high power stability (Coherent Prometheus 100NE) and was focused close to the bottom surface (i.e. the one incorporating the NV layer) of the diamond sample through an air objective (Olympus UPLANFL) with Numerical Aperture $\text{NA}=0.67$. The spot size of the focused laser beam is $\sim (10 \times 10) \mu\text{m}^2$. The power of the excitation light is varied using a Neutral Density filter. An Acousto Optic Modulator (not shown in Fig. 1) after the laser source is exploited to switch on and off the laser illumination on the sample. This solution allows to shine the laser on the sample only during the measurement time, reducing the total amount of light energy delivered to the sample. This is of key importance in biological applications.

The microwave control was obtained by a commercial

microwave generator (Keysight N5172B) whose central frequency was internally modulated at $f_{\text{mod}} = 1009 \text{ Hz}$ with modulation depth $f_{\text{dev}} = 0.6 \text{ MHz}$. For simultaneous hyperfine driving, the microwave was mixed via a double-balanced mixer with a $\sim 2.16 \text{ MHz}$ sine wave to create two simultaneous driving modulated frequencies near the central frequency. The microwave generator was connected to the lock-in LIA to provide a sinusoidal reference channel modulated at f_{mod} .

A permanent magnet fixed on a translation stage, allowing micrometric movement along the three spatial axes, provided the external magnetic field applied to the diamond sample. An additional coil (not shown in Fig. 1) provided magnetic field modulation. The coil is aligned along the vertical z-direction, in this way the modulated additional field has the same projection along all the four possible orientation of the NV axis.

The photoluminescence (PL) emission was spectrally filtered with a notch filter and a long-pass filter both centered at 650 nm, then collected and detected with two different acquisition systems. A 4% fraction of the total PL intensity was sent to a single-photon detector (SPD). The signal from the SPD was used for the ODMR spectrum acquisition. The remaining 96% fraction of the emitted PL intensity was collected by $\text{NA}=0.25$ objective (Olympus 10x) and imaged onto a photodetector (Thorlabs DET 10A2). The signal from the photodiode was sent to the input channel of the LIA.

The time constant of the LIA was set to $\tau = 10 \text{ ms}$ for the construction of the LIA spectrum. While scanning the microwave, 20 independent measurements of the LIA signal were acquired. In the measurement of the Linear Spectral Density (LSD) of the noise, a time constant of $\tau = 1 \text{ ms}$ was set. For the estimation of LSD, we acquired the LIA signal for 10 minutes with a sampling rate of $s = 5000 \text{ Hz}$ and subsequently the LIA signal was Fast-Fourier transformed.

II. RESULTS

Figure 2(a) depicts the LIA signal in function of the microwave frequency. Three frequency ranges can be identified over which the LIA signal is directly proportional to the resonance shift and hence to the applied field. A yellow dashed rectangle encloses the central one. These three zones correspond to the three dips in the ODMR spectrum due to the hyperfine coupling of the NV electronic system with the ^{14}N nuclear spin. The LIA signal is linear in these zones because the LIA detection method is sensitive to the first derivative of the ODMR spectrum.

The figure of merit of the LIA detection method is represented by the slope b of the curve in the linear zone, as reported in in Fig. 2(a). In this zone, δB_{NV} is related to the measured LIA signal S_{LIA} by²¹ by:

$$\delta B_{\text{NV}} = \frac{h}{g\mu_B} \delta\nu_+ = \frac{h}{g\mu_B} \frac{1}{b} S_{\text{LIA}}. \quad (2)$$

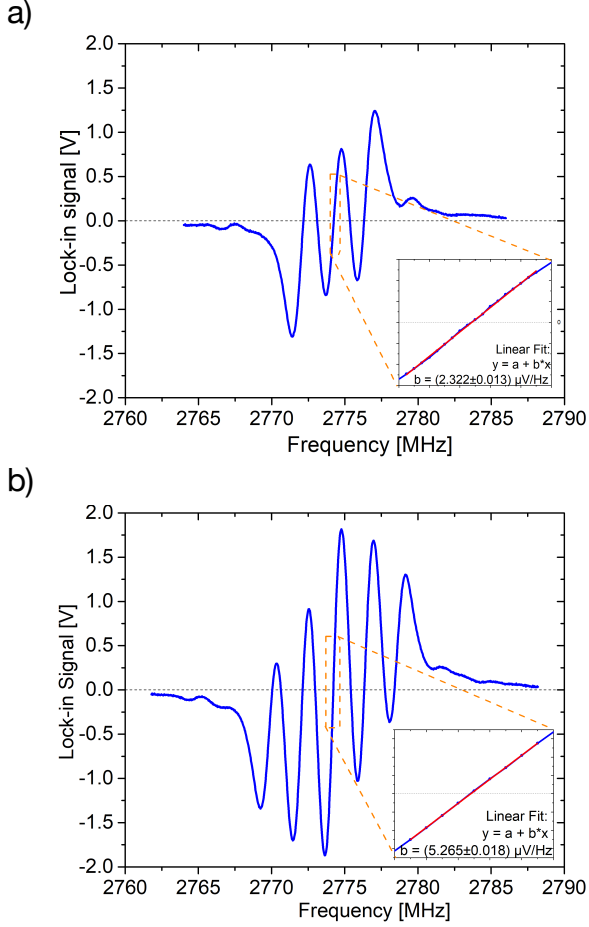


FIG. 2: Lock-in spectrum with excitation of a single resonance (a) and simultaneous excitation of the three resonances separated by the hyperfine coupling (b). The insets shows the central linear zone and the value b of the slope the curve.

It is possible to increase the slope of the curve (and thus the sensitivity of the technique) by simultaneously addressing all the three resonances^{21,25}. To this scope, three frequency-modulated microwave tones separated by the hyperfine splitting $A_{orth} = 2.16$ MHz are generated. When the center tone is at the frequency of the center resonance, all three resonance are excited, thus enhancing the slope of the curve. Fig. 2(b) shows an example of the LIA spectrum for multiple frequency excitation. b is increased by a factor ≈ 2 compared to single-tone excitation.

The minimum detectable field B_{min} is

$$B_{min} = \frac{h}{g\mu_B} \frac{1}{b} \frac{\sigma_S}{\sqrt{N}}, \quad (3)$$

where we have considered N independent measurements and that S_{LIA} is affected by an uncertainty equal to σ_S . Increasing the total time of measurement T leads to the

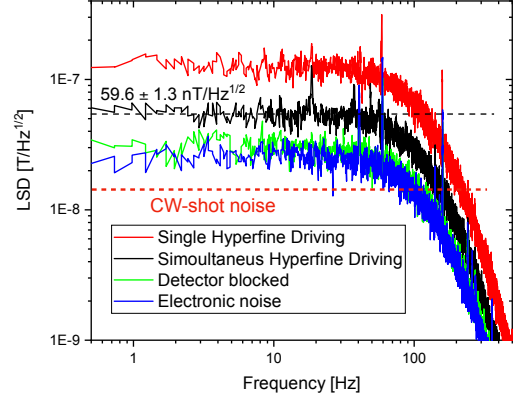


FIG. 3: Comparison between the linear spectral densities (LSD) of the readout of the NV sensor in single hyperfine driving regime (red line) and in the simultaneous hyperfine driving (black line). The linear spectral density of the read-out with the detector blocked (green line), with the input of the LIA disconnected (blue line) and the Continuous Wave (CW)-shot noise (red dashed line) are also shown.

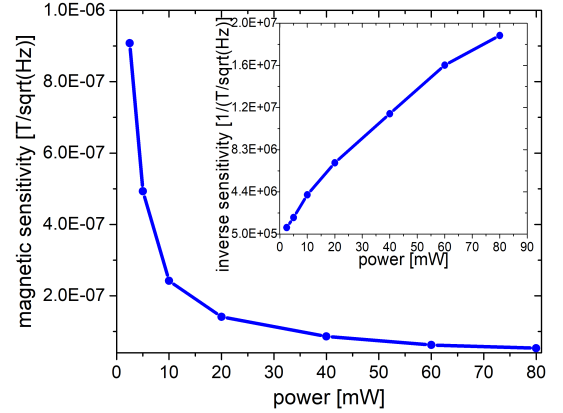


FIG. 4: Magnetic Sensitivity for different values of the applied optical power. In the inset, the inverse of the sensitivity is shown for the same power values.

usual scaling of the sensitivity η :

$$\eta = B_{min} \sqrt{T} = \frac{h}{g\mu_B} \frac{1}{b} \frac{\sigma_S}{\sqrt{N}} \sqrt{T}, \quad (4)$$

Fig. 3 shows the Linear Spectral Density of the LIA noise multiplied by the factor $\frac{g\mu_B \Delta\nu}{b}$, as defined in equation Eq. 3. For the Lock-in detection scheme described in this work, η corresponds to the low-frequency plateau in Fig. 3. Fig. 3 also shows the shot-noise limit for the single hyperfine driving. The Continuous Wave (CW) shot-noise limit is:

$$\eta_{CW} = \frac{h}{g\mu_B} \frac{\sqrt{I_0}}{\max\left(\frac{\partial I_0}{\partial \nu}\right)} \quad (5)$$

We estimated it from ODMR spectrum as follow:

$$\eta_{CW} = K \frac{h}{g\mu_B} \frac{\Delta\nu}{2\sqrt{I_0}C} = 14 \text{ nT/Hz}^{1/2} \quad (6)$$

where $\Delta\nu = 2.599 \text{ MHz}$ is the linewidth, $C = 0.006$ the contrast for the central dip of the hyperfine spectrum and $K = 0.31$ is a specific constant of this line. $I_0 = 3.03 \cdot 10^{10} \text{ s}^{-1}$ is estimated from the optical power incident onto the photodiode $W = 8.5 \text{ nW}$, considering a photon energy $E_{ph} = 2.84 \cdot 10^{-19} \text{ J}$.

Fig. 3 shows that simultaneous driving improves the sensitivity by a factor of ≈ 2 . This improvement is due to two contributions: (i) an increase in the slope b by a factor ≈ 2 (ii) no significant increase in the LIA noise.

To point out the biocompatibility of this method, we measured the magnetic sensitivity for different applied powers, see Fig. 4. The sensitivity decreased by lowering the laser power. There is a tradeoff between laser power reduction that improves biocompatibility and sensitivity that will be discussed in detail in the next section. In the next section, we will discuss which maximum power a biological system can bear.

III. DISCUSSION

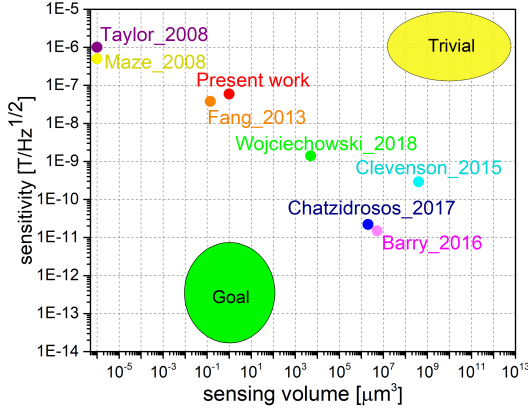


FIG. 5: The sensitivity in function of the sensing volume for the present study and from data taken from literature [NV²⁶, ND 2008²⁷, Fang 2013²⁸, Barry 2016²¹, Wojciechowski 2018²⁹, Clevenson 2015³⁰, Chatzidrosos 2017³¹]. The region of interest for biological application is defined by the green region

Here presented method is in principle able to resolve the contribution of a single cell to the magnetic field considering the fact that in our demonstrated case the sensing volume is defined by the laser spot in x-y plane of $(10 \times 10) \mu\text{m}^2$, and the thickness of NV-rich layer of 10 nm (along z-axis).

We obtained a sensitivity of $\eta = 59.6 \pm 1.3 \text{ nT}/\sqrt{\text{Hz}}$ for an optical power of 80 mW: this value is beyond (or at

least well comparable) with the one obtained in previous works if the sensing volume is taken in account^{21,29–31}, see Fig.5. Nonetheless, it has to be underlined that it is not proved that living cells can sustain 80 mW of power radiating on a surface of $100 \mu\text{m}^2$, even considering that we apply this power only for a measurement time of 10 ms in a measurement cycle of 1 s. On the other end, living neuronal cells can surely tolerate without being affected a power of 3 mW applied for minutes in the same optical geometry of our setup¹³. Considering that we apply the optical power only for few milliseconds, we can estimate a conservative biocompatible optical power $\geq 10 \text{ mW}$, that results in a sensitivity around $\eta_{bio} \leq 200 \text{ nT}/\sqrt{\text{Hz}}$.

This value of sensitivity still needs to be increased to sense neuron (or hearth cells) activity, where we expect a 1-10 nT in proximity of a single channel (a functionalised nanodiamond can in principle be targeted at nanometric distance from the channel) or when considering tissue slices. Furthermore, ion channels clustering can further increase the previous values.

This is a reasonable improvement with present techniques: Barry et al.²¹ estimated that a 300-fold improvement could be achieved using pulse sequences and new techniques in sample preparation. The main advantages offered by pulsed techniques are³²: (i) the possibility of working in a high-optical-intensity regime (ii) the possibility of taking advantage of a elongated coherence time T_2^* . Also considering this improvement, a factor five is still needed to achieve the magnetic sense of the heart activity. The use of a heat-sink and of a reflective layer could allow the adoption of higher optical powers and thus reach the desired sensitivity.

IV. CONCLUSIONS

We presented an experimental apparatus and sensing protocol compatible with the measurement of magnetic fields in biological systems at an intracellular/cellular scale, and with a sensitivity beyond previous works. These results indicate a clear strategy for magnetic sensing at cellular level, contributing to paving the way to practical biological applications of these methods. Nevertheless, it must be emphasized that due to the small, potentially at nanoscale, volume of our technique, this can find a broad application, beyond the biological example that we have discussed

Availability of data and materials

All the experimental data presented are available from the authors upon reasonable request.

Funding

This work has received funding from the European Union's PATHOS EU H2020 FET-OPEN grant no. 828946 and Horizon 2020, from the EMPIR Participating States in the context of the projects EMPIR-17FUN06 "SIQUEST" and from the project Piemonte Quantum Enabling Technologies (PiQuET) funded by the Piemonte Region.

Acknowledgements

The authors wish to thank Elio Bertacco for the technical help in implementing the frequency modulation and Giulia Tomagra for the interesting discussions about the biocompatibility of the setup.

-
- ¹ Jinhu Xiong, Peter T Fox, and Jia-Hong Gao. Directly mapping magnetic field effects of neuronal activity by magnetic resonance imaging. *Human brain mapping*, 20(1):41–49, 2003.
 - ² Bingshuo Li, Juha P Virtanen, Axel Oeltermann, Cornelius Schwarz, Martin A Giese, Ulf Ziemann, and Alia Benali. Lifting the veil on the dynamics of neuronal activities evoked by transcranial magnetic stimulation. *Elife*, 6:e30552, 2017.
 - ³ Dimitri M Kullmann. Neurological channelopathies. *Annual review of neuroscience*, 33:151–172, 2010.
 - ⁴ Bernd Kuhn, Federico Picollo, Valentina Carabelli, Giorgio Rispoli. Advanced real time recordings of neuronal activity *Pflgers Archiv European Journal of Physiology*, submitted.
 - ⁵ Stephen G Waxman. Axonal conduction and injury in multiple sclerosis: the role of sodium channels. *Nature Reviews Neuroscience*, 7(12):932–941, 2006.
 - ⁶ Giulia Tomagra, Federico Picollo, Alfio Battiato, Barbara Picconi, Silvia De Marchis, Alberto Pasquarelli, Paolo Olivero, Andrea Marcantoni, Paolo Calabresi, Emilio Carbone, et al. Quantal release of dopamine and action potential firing detected in midbrain neurons by multifunctional diamond-based microarrays. *Frontiers in neuroscience*, 13, 2019.
 - ⁷ David Cohen. Magnetic fields around the torso: production by electrical activity of the human heart. *Science*, 156(3775):652–654, 1967.
 - ⁸ Annette Wacker-Gusmann, Janette F Strasburger, Bettina F Cuneo, and Ronald T Wakai. Diagnosis and treatment of fetal arrhythmia. *American journal of perinatology*, 31(07):617–628, 2014.
 - ⁹ MI Faley, U Poppe, K Urban, DN Paulson, and RL Fagaly. A new generation of the hts multilayer dc-squid magnetometers and gradiometers. In *Journal of Physics: Conference Series*, volume 43, page 1199. IOP Publishing, 2006.
 - ¹⁰ F Baudenbacher, LE Fong, JR Holzer, and M Radparvar. Monolithic low-transition-temperature superconducting magnetometers for high resolution imaging magnetic fields of room temperature samples. *Applied Physics Letters*, 82(20):3487–3489, 2003.
 - ¹¹ Shu-Jung Yu, Ming-Wei Kang, Huan-Cheng Chang, Kuan-Ming Chen, and Yueh-Chung Yu. Bright fluorescent nanodiamonds: no photobleaching and low cytotoxicity. *Journal of the American Chemical Society*, 127(50):17604–17605, 2005.
 - ¹² Ying Zhu, Jing Li, Wenxin Li, Yu Zhang, Xiaofeng Yang, Nan Chen, Yanhong Sun, Yun Zhao, Chunhai Fan, and Qing Huang. The biocompatibility of nanodiamonds and their application in drug delivery systems. *Theranostics*, 2(3):302, 2012.
 - ¹³ Laura Guarina, C Calorio, D Gavello, E Moreva, P Traina, A Battiato, S Ditalia Tchernij, J Forneris, M Gai, F Piccolo, et al. Nanodiamonds-induced effects on neuronal firing of mouse hippocampal microcircuits. *Scientific Reports*, 8(1):1–14, 2018.
 - ¹⁴ Amanda M Schrand, Houjin Huang, Cataleya Carlson, John J Schlager, Eiji Ōsawa, Saber M Hussain, and Liming Dai. Are diamond nanoparticles cytotoxic? *The journal of physical chemistry B*, 111(1):2–7, 2007.
 - ¹⁵ Kuang-Kai Liu, Chia-Liang Cheng, Chia-Ching Chang, and Jui-I Chao. Biocompatible and detectable carboxylated nanodiamond on human cell. *Nanotechnology*, 18(32):325102, 2007.
 - ¹⁶ A Gruber, A Dräbenstedt, C Tietz, L Fleury, J Wrachtrup, and C Von Borczyskowski. Scanning confocal optical microscopy and magnetic resonance on single defect centers. *Science*, 276(5321):2012–2014, 1997.
 - ¹⁷ Philipp Neumann, Johannes Beck, Matthias Steiner, Florian Rempp, Helmut Fedder, Philip R Hemmer, Jörg Wrachtrup, and Fedor Jelezko. Single-shot readout of a single nuclear spin. *Science*, 329(5991):542–544, 2010.
 - ¹⁸ Lucio Robledo, Lilian Childress, Hannes Bernien, Bas Hensen, Paul FA Alkemade, and Ronald Hanson. High-fidelity projective read-out of a solid-state spin quantum register. *Nature*, 477(7366):574–578, 2011.
 - ¹⁹ L Childress, MV Gurudev Dutt, JM Taylor, AS Zibrov, F Jelezko, J Wrachtrup, PR Hemmer, and MD Lukin. Coherent dynamics of coupled electron and nuclear spin qubits in diamond. *Science*, 314(5797):281–285, 2006.
 - ²⁰ Loïc Rondin, Jean-Philippe Tetienne, Thomas Hingant, Jean-François Roch, Patrick Maletinsky, and Vincent Jacques. Magnetometry with nitrogen-vacancy defects in diamond. *Reports on progress in physics*, 77(5):056503, 2014.
 - ²¹ John F Barry, Matthew J Turner, Jennifer M Schloss, David R Glenn, Yuyu Song, Mikhail D Lukin, Hongkun Park, and Ronald L Walsworth. Optical magnetic detection of single-neuron action potentials using quantum defects in diamond. *Proceedings of the National Academy of Sciences*, 113(49):14133–14138, 2016.
 - ²² Helen A McNally, Bartek Rajwa, Jennie Sturgis, and J Paul Robinson. Comparative three-dimensional imaging of living neurons with confocal and atomic force microscopy. *Journal of neuroscience methods*, 142(2):177–184, 2005.
 - ²³ Rolf Simon Schoenfeld and Wolfgang Harneit. Real time

- magnetic field sensing and imaging using a single spin in diamond. *Physical review letters*, 106(3):030802, 2011.
- ²⁴ Kento Sasaki, Yasuaki Monnai, Soya Saijo, Ryushiro Fujita, Hideyuki Watanabe, Junko Ishi-Hayase, Kohei M Itoh, and Eisuke Abe. Broadband, large-area microwave antenna for optically detected magnetic resonance of nitrogen-vacancy centers in diamond. *Review of Scientific Instruments*, 87(5):053904, 2016.
 - ²⁵ Haitham AR El-Ella, Sepehr Ahmadi, Adam M Wojciechowski, Alexander Huck, and Ulrik L Andersen. Optimised frequency modulation for continuous-wave optical magnetic resonance sensing using nitrogen-vacancy ensembles. *Optics express*, 25(13):14809–14821, 2017.
 - ²⁶ JM Taylor, P Cappellaro, L Childress, L Jiang, D Budker, PR Hemmer, A Yacoby, R Walsworth, and MD Lukin. High-sensitivity diamond magnetometer with nanoscale resolution. *Nature Physics*, 4(10):810–816, 2008.
 - ²⁷ Jeronimo R Maze, Paul L Stanwix, James S Hodges, Seungpyo Hong, Jacob M Taylor, Paola Cappellaro, Liang Jiang, MV Gurudev Dutt, Emre Togan, AS Zibrov, et al. Nanoscale magnetic sensing with an individual electronic spin in diamond. *Nature*, 455(7213):644–647, 2008.
 - ²⁸ Kejie Fang, Victor M Acosta, Charles Santori, Zhihong Huang, Kohei M Itoh, Hideyuki Watanabe, Shinichi Shikata, and Raymond G Beausoleil. High-sensitivity magnetometry based on quantum beats in diamond nitrogen-vacancy centers. *Physical review letters*, 110(13):130802, 2013.
 - ²⁹ Adam M Wojciechowski, Mürsel Karadas, Christian Osterkamp, Steffen Jankuhn, Jan Meijer, Fedor Jelezko, Alexander Huck, and Ulrik L Andersen. Precision temperature sensing in the presence of magnetic field noise and vice-versa using nitrogen-vacancy centers in diamond. *Applied Physics Letters*, 113(1):013502, 2018.
 - ³⁰ Hannah Clevenson, Matthew E Trusheim, Carson Teale, Tim Schröder, Danielle Braje, and Dirk Englund. Broadband magnetometry and temperature sensing with a light-trapping diamond waveguide. *Nature Physics*, 11(5):393–397, 2015.
 - ³¹ Georgios Chatzidrosos, Arne Wickenbrock, Lykourgos Bougas, Nathan Leefer, Teng Wu, Kasper Jensen, Yannick Dumeige, and Dmitry Budker. Miniature cavity-enhanced diamond magnetometer. *Physical Review Applied*, 8(4):044019, 2017.
 - ³² John F Barry, Jennifer M Schloss, Erik Bauch, Matthew J Turner, Connor A Hart, Linh M Pham, and Ronald L Walsworth. Sensitivity optimization for nv-diamond magnetometry. *Reviews of Modern Physics*, 92(1):015004, 2020.